

# A Multidimensional Dependence of the Substructure Evolution on the Tidal Coherence

Jounghun Lee

*Astronomy Program, Department of Physics and Astronomy, Seoul National University,  
Seoul 08826, Republic of Korea*

jounghun@astro.snu.ac.kr

## ABSTRACT

We numerically explore how the subhalo mass-loss evolution is affected by the tidal coherences measured along different eigenvector directions. The mean virial-to-accretion mass ratios of the subhalos are used to quantify the severity of their mass-loss evolutions within the hosts, and the tidal coherence is expressed as an array of three numbers each of which quantifies the alignment between the tidal fields smoothed on the scales of 2 and  $30 h^{-1} \text{Mpc}$  in each direction of three principal axes. Using a Rockstar halo catalog retrieved from a N-body simulation, we investigate if and how the mass-loss evolutions of the subhalos hosted by distinct halos at fixed mass scale of  $[1-3]10^{14} h^{-1} M_{\odot}$  are correlated with three components of the tidal coherence. The tides coherent along different eigenvector directions are found to have different effects on the subhalo mass-loss evolution, which cannot be ascribed to the differences in the densities and ellipticities of the local environments. It is shown that the substructures surrounded by the tides highly coherent along the first eigenvector direction and highly *incoherent* along the third eigenvector direction experience the least severe mass-loss evolution, while the tides highly *incoherent* only along the first eigenvector direction is responsible for the most severe mass-loss evolution of the subhalos. Explaining that the coherent tides have an obstructing effect on the satellite infalls onto their hosts and that the strength of the obstruction effect depends on which directions the tides are coherent or *incoherent* along, we suggest that the multidimensional dependence of the substructure evolution on the tidal coherence should be deeply related to the complex nature of the large-scale assembly bias.

*Subject headings:* cosmology:theory — large-scale structure of universe

## 1. Introduction

The classical excursion set theory based on the standard  $\Lambda$ CDM (cosmological constant  $\Lambda$  and cold dark matter) model provided an analytical framework within which the formation and evolution of DM halos, the building blocks of the large-scale structure in the universe, can be physically tracked down (Press, & Schechter 1974; Bardeen et al. 1986; Bond et al. 1991; Bond, & Myers 1996; Sheth et al. 2001). According to this theory, the hierarchical accretion and merging events, which are the dominant driver of the halo growth, owe their frequencies solely to the halo masses. N-body simulations that were performed to complement the theory with desired accuracy and precision, however, invalidated this simple picture, discovering a puzzling phenomenon, so called the "halo assembly bias": The clustering strength of the DM halos affect their formation epochs and growth rates on the same mass scale (Gao & White 2007). Although the discovery of this phenomenon baffled for long the community of the large-scale structure, it is now generally accepted that the cosmic web, anisotropic large-scale tidal environments surrounding DM halos (Bond et al. 1996), must be mainly responsible for the deviation of the simple prediction of the excursion set theory on the halo growths from the reality (e.g., Sandvik et al. 2007; Hahn et al. 2009; Wang et al. 2011; Borzyszkowski et al. 2017; Tojeiro et al. 2017; Yang et al. 2017; Musso et al. 2018; Mansfield, & Kravtsov 2019; Ramakrishnan et al. 2019). Thus, a key to understanding the halo assembly bias is to figure out what aspect of the anisotropic tidal fields affects the halo growths.

The cosmic web is further classified into four different types each of which has a distinct geometrical shape and dimension: zero dimensional knots, one dimensional filaments, two dimensional walls and three dimensional voids (Hahn et al. 2007). Among them, the most anisotropic web-type, the filament, turned out to embed the majority of DM halos (e.g., Ganeshiah Veena et al. 2019) which were believed to grow via the preferential merging and accretion of satellites along the narrow one-dimensional channels (e.g., West et al. 1995; Plionis, & Basilakos 2002; Vera-Ciro et al. 2011). A recent numerical work of Borzyszkowski et al. (2017) based on a high-resolution N-body simulation, however, revealed that the motions of satellites confined in the filamentary environments could have opposite effects on the growths of galactic halos, depending on the filament thickness (see also González, & Padilla 2016). If multiple fine filaments cross one another at some nodes, the radial motions of the satellites along the filaments facilitate their infalls onto the galactic halos located at the nodes, enhancing the growths of the hosts. Whereas, in the bulky filaments thicker than the sizes of the constituent galactic halos, the satellites preferentially move in the tangential directions orthogonal to the filament axes, which lead to the deterrence of the satellite infalls and the retarded growths of their hosts. Quantifying the filament thickness in terms of the ellipticity of the surrounding large-scale structure and incorporat-

ing it into the conditions for the halo formation, Borzyszkowski et al. (2017) proposed a new extension of the excursion set theory which could accommodate the opposite effects of the large-scale tidal environments on the growths of the galactic halos (see also Garaldi et al. 2017).

Motivated by the insightful work of Borzyszkowski et al. (2017), several attempts were made to improve their model by incorporating more realistic conditions from the halo growths or by extending the model to the larger scales or to the other web types (Lazeyras et al. 2017; Musso et al. 2018; Lee 2019). For instance, Lee (2019) introduced a new concept of the "tidal coherence" for a quantitative explicit description of the filament thickness, suggesting that bulky thick (multiple fine) filaments should be outcomes of the highly coherent (*incoherent*) tides defined as the strong (weak) alignments between the first eigenvectors corresponding to the largest eigenvalues of the tidal fields smoothed on two widely separated scales. With the numerical analysis on the cluster scales, Lee (2019) indeed found that the radial (tangential) motions of the infall-zone satellites around host clusters are obstructed (facilitated) by the highly coherent tides, which implies that the halo growth sensitively depends on the degree of the tidal coherence.

Yet, the prime focus of Lee (2019) was the future evolution of the cluster halos rather than their past evolutions, dealing with the infall-zone satellites which have yet to fall into the halos. It is necessary to treat the real satellites for the investigation of the effect of the tidal coherence on the past growths of the DM halos. Besides, the original definition of the tidal coherence in terms only of the first eigenvector direction may neglect the possibilities that the coherence in the second and third eigenvector directions corresponding to the second largest and smallest eigenvalues are not evinced by the coherence in the first eigenvector direction and that the simultaneous coherence of the tides in multiple eigenvector directions may have different effects on the halo growths.

In this Paper, we attempt to incorporate the multi-dimensional aspect of the tidal coherence into the idea of Lee (2019) and to explore how it affects the halo growths by measuring a correlation between the mass-loss evolution of the halo satellites and the multi-dimensional tidal coherence. In Section 2.1 the definition of the multi-dimensional tidal coherence as well as the description of the numerical data sets utilized for this analysis are presented. In Sections 2.2-2.4, the effects of the simultaneous coherence of the tides along one, two and three eigenvector directions on the subhalo mass-loss evolutions are presented. In Section 3 the final results are summarized and its implication on the halo assembly bias is discussed. Throughout this analysis, we will assume a concordance cosmology with initial conditions prescribed by the Planck result (Planck Collaboration et al. 2014).

## 2. Dependence of the Satellite Mass-Loss on the Tidal Coherence

### 2.1. Tidal Coherence as a Multi-Component Array

For this analysis, we utilize the catalog of the Rockstar halos (Behroozi et al. 2013) and density field at  $z = 0$  retrieved from the website of the Small MultiDark Planck simulation<sup>1</sup>(SMDPL, Klypin et al. 2016), a DM-only N-body simulation performed on a periodic box of linear size  $400 h^{-1}\text{Mpc}$ , containing  $3840^3$  DM particles of individual mass  $m_p = 9.63 \times 10^7 h^{-1} M_\odot$  for the Planck cosmology (Planck Collaboration et al. 2014). The catalog contains both of the distinct halos and the subhalos, which can be distinguished by their parent ID (pId): The former has pId=  $-1$  while the pId of the latter is nothing but the ID of its parent halo, a least massive distinct halo which gravitationally hosts the latter. Selecting as the hosts the massive cluster-size distinct halos in the mass range of  $(1 - 3)10^{14} h^{-1} M_\odot$ , we identify their subhalos whose pId’s match their ID’s.

For each subhalo belonging to each host, we determine the ratio,  $\xi_m \equiv M_{\text{vir}}/M_{\text{acc}}$ , of its virial mass,  $M_{\text{vir}}$ , to its accretion mass,  $M_{\text{acc}}$ , defined as the subhalo mass at the moment of its accretion to its host. The majority of the subhalos are to lose their masses after their infalls via various processes like the tidal stripping/heating and dynamical frictions (van den Bosch et al. 2005), for which cases we expect  $\xi_m < 1$ . The lower value of  $\xi_m$  below unity indicates that the given subhalo must have experienced the severe mass-loss processes for longer time after the infall. Yet, in some rare occasions, the subhalos can gain masses through merging inside the hosts for which case  $\xi_m$  can exceed unity. From here on, two terms, *subhalos* and *satellites*, will be interchangeably used to refer to the non-distinct Rockstar halos gravitationally bound to some larger distinct halos.

As done in Lee (2019), we compute the tidal field,  $T_{ij}(\mathbf{x})$ , from the density field defined on the  $512^3$  grid points,  $\rho(\mathbf{x})$ , by taking the following steps: (i) Calculating the density contrast field as  $\delta(\mathbf{x}) \equiv (\rho(\mathbf{x}) - \bar{\rho})/\bar{\rho}$  where  $\bar{\rho}$  is the mean density averaged over the grid points. (ii) Performing the Fourier transformation of  $\delta(\mathbf{x})$  into  $\tilde{\delta}(\mathbf{k})$ . (iii) Smoothing the density field in the Fourier space with a Gaussian filter on the scale of  $R_f = 30 h^{-1}\text{Mpc}$  as  $\tilde{\delta}_s(\mathbf{k}) \equiv \tilde{\delta}(\mathbf{k}) \exp(-k^2 R_f^2/2)$ . (iv) Computing the Fourier amplitude of the tidal field as  $\tilde{T}_{ij} \equiv k_i k_j \tilde{\delta}_s(\mathbf{k})/k^2$ . (v) Performing the inverse Fourier transformation of  $\tilde{T}_{ij}(\mathbf{k})$  into  $T_{ij}(\mathbf{x})$ . At the grid point,  $\mathbf{x}_h$ , where each of the selected hosts is located, we diagonalize  $T_{ij}(\mathbf{x}_h)$  to find a set of three eigenvalues  $\{\lambda_i\}_{i=1}^3$  (with a decreasing order) and the corresponding eigenvectors  $\{\mathbf{e}_i\}_{i=1}^3$ . Then, we repeat the whole process but with a smaller filtering scale of  $R'_f = 2 h^{-1}\text{Mpc}$  to obtain a new set of  $\{\lambda'_i\}_{i=1}^3$  and  $\{\mathbf{e}'_i\}_{i=1}^3$ .

---

<sup>1</sup><https://www.cosmosim.org>

As mentioned in Section 1, the tidal coherence,  $q$ , was originally defined as  $q \equiv |\mathbf{e}_1 \cdot \mathbf{e}'_1|$  (Lee 2019). In the current work, we redefine  $q$  as a multi-component array as

$$q_i = |\mathbf{e}_i \cdot \mathbf{e}'_i| \quad \text{for each } i \in \{1, 2, 3\}. \quad (1)$$

If  $q_i$  is equal to or higher than 0.9 (lower than 0.2) at a given region, the tides is said to be highly coherent (*incoherent*) along the  $i$ th eigenvector direction at the region. A critical question to which we would like to find an answer in the following Subsections is whether or not the subhalos located in the regions where the tides are highly coherent or *incoherent* in different eigenvector directions exhibit different mass-loss evolutions.

## 2.2. One Dimensional Dependence

In this Subsection, we are going to study how the mean value of the subhalo virial-to-accretion mass ratios depends on each of the three components of the tidal coherence,  $\{q_i\}_{i=1}^3$ , calling it one-dimensional (1D) dependence of the subhalo mass-loss evolution on the tidal coherence. We first divide the sample of the selected host halos into two subsamples: One contains those hosts surrounded by the tides highly coherent along the first eigenvector direction, satisfying the condition of  $q_1 \geq 0.9$ . The other consists of those surrounded by the tides not so strongly coherent along the first eigenvector direction with  $q_1 < 0.9$ . Table 1 lists the mean masses ( $\langle M_h \rangle$ ) and numbers ( $N_h$ ) of the hosts contained in each subsample. As can be seen, although the latter subsample (i.e.,  $q_1 < 0.9$ ) contains three times larger number of hosts, no significant difference in  $\langle M_h \rangle$  between the two subsamples is noted, which assures that if the values of  $\langle \xi_m \rangle$  from the two subsamples are significantly different from each other, then it should not be ascribed to the mass difference.

For each host contained in each subsample, we select only those subhalos which experienced the *mass-loss* process, i.e.,  $\xi_m < 1$ , excluding those few subhalos which experienced the mass-gain process,  $\xi_m \geq 1$ . Then, we calculate the mean virial-to-accretion mass ratio,  $\langle \xi_m \rangle$ , averaged over the selected subhalos of the hosts contained in each subsample. The errors,  $\sigma_{\xi_m}$ , in the measurement of  $\langle \xi_m \rangle$ , is calculated as its standard deviation as  $\sigma_{\xi_m} \equiv [(\langle \xi_m \rangle - \langle \xi_m \rangle)^2 / (N_{\text{sub}} - 1)]^{1/2}$  where  $N_{\text{sub}}$  is the total number of the subhalos of the hosts contained in each subsample.

Figure 1 plots the values of  $\langle \xi_m \rangle$  from the two subsamples with  $q_1 \geq 0.9$  and  $q_1 < 0.9$  as thick red and blue bars, respectively, with the associated errors  $\sigma_{\xi_m}$  in its left panel, explicitly demonstrating that the former yields a significantly higher value of  $\langle \xi_m \rangle$  than the latter. This trend implies that the satellites located in the regions surrounded by the tides highly coherent along the first eigenvector direction experience less severe mass-loss

evolution after their infalls onto their hosts than the other counterparts with  $q_1 < 0.9$ . Based on the insights from Lee (2019), we put forth the following explanation to understand this phenomenon: As the satellites surrounded by highly coherent tides along the first eigenvector direction develop velocities in the tangential direction, which deter their infalls onto the hosts, reducing the amount of time during which the subhalos are exposed to the effects of the tidal stripping/heating or dynamical friction inside their hosts.

Repeating the above procedure but with the subsamples obtained by constraining the value of  $q_2$  ( $q_3$ ) instead of  $q_1$  with the same threshold of 0.9, we also investigate how  $\langle \xi_m \rangle$  differs between the cases of  $q_2 \geq 0.9$  and  $q_2 < 0.9$  ( $q_3 \geq 0.9$  and  $q_3 < 0.9$ ). The middle (right) panel of Figure 1 plots the same as the left panel but for the case that the subsample is divided by imposing the threshold condition on the value of  $q_2$  ( $q_3$ ). As can be seen, the subhalos of the hosts located in the regions with  $q_2 \geq 0.9$  ( $q_3 \geq 0.9$ ) yield a larger value of  $\langle \xi_m \rangle$  than those with  $q_2 < 0.9$  ( $q_3 < 0.9$ ), the same trend as that shown in the left panel of Figure 1. Note, however, that the larger (smaller) difference in  $\langle \xi_m \rangle$  between the two subsamples are found for the case that the threshold condition is imposed on the value of  $q_3$  ( $q_2$ ) rather than on the value of  $q_1$ .

To see whether or not this difference in  $\langle \xi_m \rangle$  witnessed in Figure 1 is a secondary effect induced by any differences in the local density ( $\delta$ ) or ellipticity ( $e$ ) between the two subsamples, we determine the values  $\delta$ , and  $e$  at the grid point of each host. The three tidal eigenvalues,  $\{\lambda'_i\}_{i=1}^3$  on the scale of  $2 h^{-1} \text{Mpc}$  obtained in Subsection 2.1 is used to calculate  $\delta$  and  $e$ :  $\delta = \sum_{i=1}^3 \lambda'_i$ , and  $e \equiv [(1 + \delta)^{-1} \sum_{i < j} (\lambda'_i - \lambda'_j)^2]^{1/2}$ . This definition of  $e$ , was devised by Ramakrishnan et al. (2019) to eliminate any correlation between  $e$  and  $\delta$ .

Taking the mean values,  $\langle \delta \rangle$  and  $\langle e \rangle$ , averaged over all hosts contained in each of the subsamples, we plot them in the top and bottom panels of Figure 2, respectively. As can be seen, when the value of  $q_2$  or  $q_3$  are constrained by using a threshold of 0.9, no significant differences are found in  $\langle \delta \rangle$  and  $\langle e \rangle$  between the two subsamples. Whereas, the subsample with  $q_1 \geq 0.9$  is found to have substantially larger values of  $\langle \delta \rangle$  and  $\langle e \rangle$  than the other subsample with  $q_1 < 0.9$ . That is, the regions surrounded by the tides highly coherent along the first eigenvectors tend to be more overdense and more anisotropic due to the simultaneous compression of matter along the coherent first eigenvector direction. This result brings out a suspicion that the higher value of  $\langle \xi_m \rangle$  found in the subsample with  $q_1 \geq 0.9$  may be caused by the higher values of  $\langle \delta \rangle$  and  $\langle e \rangle$ .

Now that the tides highly coherent along the eigenvector direction are found to have an obstruction effect on the satellite infalls, the next quest is to investigate whether the tides highly *incoherent* along any eigenvector direction have the opposite effect or not. For this quest, we use two thresholds: an upper-bound threshold of 0.2 and a lower-bound threshold

of 0.9 to construct two subsamples (i.e.,  $q_i \geq 0.9$  and  $q_i < 0.2$  for each  $i \in \{1, 2, 3\}$ ) and then conduct the same analysis. Figures 3-4 plot the same as Figures 1-2, respectively, but with the conditions of  $q_i \geq 0.9$  and  $q_i < 0.2$  instead of  $q_i \geq 0.9$  and  $q_i < 0.9$ . The left panel of Figure 3 reveals that the difference in  $\langle \xi_m \rangle$  between the two subsamples obtained by putting two thresholds of 0.9 and 0.2 on the value of  $q_1$  is larger than that by putting one threshold of 0.9. This result indicates that the tides highly *incoherent* along the first eigenvector direction indeed have the opposite effect on the satellite infalls: it facilitates the satellite infalls onto the hosts, leading them to undergo the more severe mass-loss evolution after the infalls. Meanwhile, the left panel of Figure 4 shows that the difference in  $\langle \delta \rangle$  and  $\langle e \rangle$  between the two subsamples obtained by putting two thresholds of 0.9 and 0.2 on the value of  $q_1$  is smaller than that by using one threshold of 0.9, which proves that the larger values of  $\langle \delta \rangle$  and  $\langle e \rangle$  are not mainly responsible for the more severe mass-loss evolution of the subhalos found from the subsample with  $q_1 \geq 0.9$ .

It is interesting, however, to discover in the right panel of Figure 3 that the tides highly *incoherent* along the third eigenvector direction does not have the expected opposite effect, compared to that coherent along the same direction. The difference in  $\langle \xi_m \rangle$  between the subsamples obtained by putting two thresholds of 0.9 and 0.2 on  $q_3$  is smaller than that between the subsamples obtained by putting one threshold of 0.9 on  $q_3$ . This result indicates that the tides highly *incoherent* along the third eigenvector direction have an obstructing effect on the satellite infalls rather than facilitating it unlike the tides highly *incoherent* along the first eigenvector direction. This phenomenon may be closely linked with the larger mean ellipticity,  $\langle e \rangle$ , found in the subsample with  $q_3 < 0.2$  than in the subsample with  $q_3 < 0.9$ , shown in the right panel of Figure 4. The tides highly *incoherent* along the third eigenvector direction can increase the tidal anisotropy of a region, which in turn makes it harder for the satellites in the region to fall onto their hosts. As the satellite infalls are deterred, they must go through less severe mass-loss evolution after the infalls till the present epochs. Note also in the middle panels of Figures 1-4 that the tidal coherence measured along the second eigenvector direction have the weakest effect on the subhalo mass-loss evolution, showing no significant differences in  $\langle \xi_m \rangle$ ,  $\langle \delta \rangle$ , and  $\langle e \rangle$  among three samples with  $q_2 \geq 0.9$ ,  $q_2 < 0.9$  and  $q_2 < 0.2$ .

### 2.3. Two Dimensional Dependence

Now that the surrounding tides coherent along different eigenvector directions are found to have different effects on the mass-loss evolution of the subhalos, we would like to explore the effects of the tides coherent simultaneously along two eigenvector directions. Since the

tidal coherence measured along the second eigenvector direction is found to have the weakest effect on the subhalo mass-loss evolution in Subsection 2.2, we will focus on the tidal coherence measured simultaneously along the first and third eigenvector directions (i.e.,  $q_1$  and  $q_3$ ) in this Subsection.

We first separate the selected host halos into four subsamples by simultaneously constraining the values of  $q_1$  and  $q_3$  with a single threshold of 0.9 (see Table 2). Then, we calculate  $(\langle \xi_m \rangle, \sigma_{\xi_m})$ ,  $(\langle \delta \rangle, \sigma_\delta)$  and  $(\langle e \rangle, \sigma_e)$  by taking the same steps described in Subsection 2.2 for each of the four subsamples, the results of which are displayed in Figures 5-6. As can be seen in Figure 5, the two subsamples satisfying the conditions of  $(q_1 \geq 0.9, q_3 < 0.9)$  and  $(q_1 < 0.9, q_3 \geq 0.9)$  yield significantly higher values of  $\langle \xi_m \rangle$  than the other two subsamples. A crucial implication of this result is that the tides highly coherent along the first (third) eigenvector direction but not along the third (first) eigenvector directions have a stronger obstructing effect on the satellite infalls than the tides highly coherent along both of the first and third eigenvector directions.

It is interesting to see that while the two subsamples with of  $(q_1 \geq 0.9, q_3 < 0.9)$  and  $(q_1 < 0.9, q_3 \geq 0.9)$  show no significant difference in the values of  $\langle \xi_m \rangle$  and  $\langle \delta \rangle$  from each other, a substantial difference in the value of  $\langle e \rangle$  is found between them (see Figure 6): the regions surrounded by the tides highly coherent along the first eigenvector direction but not along the third ones are more anisotropic than those surrounded by the tides highly coherent along the third eigenvector direction but not along the first ones. Given that the tidal anisotropy can also have an effect of obstructing the satellite infalls, the larger value of  $\langle \xi_m \rangle$  found from the subsample with  $q_1 \geq 0.9$  and  $q_3 < 0.9$  may be partly caused by its larger value of  $\langle e \rangle$  than that from the subsample with  $q_1 < 0.9$  and  $q_3 \geq 0.9$ . The lowest value of  $\langle \xi_m \rangle$  is found from the subsample with  $q_1 < 0.9$  and  $q_2 < 0.9$ , which indicates that the tides highly coherent along none of the first nor third eigenvector directions have the weakest obstructing and/or strongest facilitating effects of the satellite infalls.

We also investigate the effect of the highly *incoherent* tides on the subhalo mass-loss evolution and on the local density and ellipticity as well by constraining the value of  $q_1$  and  $q_3$  with double thresholds of 0.9 and 0.2, the results of which are shown in Figures 7-8. As can be seen in Figure 7, the subsample with  $q_1 \geq 0.9$  and  $q_3 < 0.2$  yields the highest value of  $\langle \xi_m \rangle$  among the four, while its lowest value is found in the subsample with  $q_1 < 0.2$  and  $q_3 \geq 0.9$ . This result indicates that the tides highly coherent along the first eigenvector direction and highly *incoherent* along the third eigenvector direction are most effective in obstructing the satellite infalls, while the tides highly coherent along the third eigenvector direction and *incoherent* along the first eigenvector direction are most effective in facilitating the infalls among the four. Given that the subsample with  $(q_1 \geq 0.9, q_3 < 0.2)$  yields



the highest value of  $\langle e \rangle$  among the four, the largest value of  $\langle \xi_m \rangle$  from the subsample with  $q_1 \geq 0.9$  and  $q_3 < 0.2$  should be partially caused by a larger value of  $\langle e \rangle$ .

It is worth recalling that in Subsection 2.2 the tides highly coherent only along the third eigenvector direction have been already found to obstruct the satellite infalls rather than facilitate them (see the right panel of Figure 1). Nevertheless, if the tides are simultaneously incoherent along the first eigenvector direction, then the facilitating effect of the tidal *incoherence* along the first eigenvector direction seem to overwhelm the obstructing effect of the tidal coherence along the third eigenvector direction, according to the result shown in Figure 3. In other words, it is the tidal *incoherence* along the first eigenvector direction that plays the most decisive dominant role of facilitating the satellite infalls, driving the largest amount of mass-loss of the subhalos in the post-infall stages.

Meanwhile, the high coherence of the tides along the first eigenvector direction seems to be synergetic with its simultaneous *incoherence* along the third eigenvector direction (see Figure 7). The subsample with  $(q_1 \geq 0.9, q_2 < 0.2)$  yields the lowest value of  $\langle \xi_m \rangle$  not only among the subsamples obtained by simultaneously constraining both of  $q_1$  and  $q_3$  but also among the subsamples obtained by constraining only one of three components of  $\{q_i\}$  (see Figure 3). Our interpretation is that the high tidal anisotropy associated with the tides highly *incoherent* along the third eigenvector direction tends to magnify the obstructing effect of the high tidal coherence along the first eigenvector direction.

## 2.4. Three Dimensional Dependence

Now that the simultaneous constraints of  $q_1$  and  $q_3$  uncovers the complex two-dimensional dependence of the subhalo mass-loss evolution on the tidal coherence, it should be legitimate to investigate how  $\langle \xi_m \rangle$  depends on all of the three components of  $\{q_i\}_{i=1}^3$ , calling it three dimensional (3D) dependence of the subhalo mass-loss evolution on the tidal coherence. We first separate the host halos into eight subsamples by constraining simultaneously the values of  $(q_1, q_2, q_3)$  with a single threshold of 0.9 (see Table 3).

Through the same procedure described in Subsection 2.2, we determine the values of  $(\langle \xi_m \rangle, \sigma_{\xi_m})$ ,  $(\langle \delta \rangle, \sigma_\delta)$  and  $(\langle e \rangle, \sigma_e)$ , for each of the eight subsamples, which are plotted in Figures 9-10. As can be seen in Figure 9, we find the highest and lowest values of  $\langle \xi_m \rangle$  from the subsamples with  $(q_1 \geq 0.9, q_2 \geq 0.9, q_3 < 0.9)$  and  $(q_1 < 0.9, q_2 \geq 0.9, q_3 \geq 0.9)$ , respectively, among the eight. In Figure 10 where the eight subsamples exhibit little difference in  $\langle \delta \rangle$  but substantial difference in  $\langle e \rangle$ , we find the highest and lowest values of  $\langle e \rangle$  from the same two subsamples, which implies that the large difference in  $\langle e \rangle$  among the

two subsamples should be linked with the large difference in  $\langle \xi_m \rangle$ .

For the case that  $q_1 \geq 0.9$  and  $q_3 < 0.9$ , the simultaneous constraint of  $q_2 \geq 0.9$  gives the highest value of  $\langle \xi_m \rangle$  (scarlet bar). Whereas, for the case that  $q_1 < 0.9$  and  $q_3 \geq 0.9$ , the same constraint of  $q_2 \geq 0.9$  yields the opposite signal, i.e., the lowest value of  $\langle \xi_m \rangle$  (green bar). Note also that the subsample with  $(q_1 < 0.9, q_2 \geq 0.9, q_3 < 0.9)$  corresponding to the tides highly coherent only along the second eigenvector direction but not along the first and third ones yields relatively low value of  $\langle \xi_m \rangle$ . This result indicates that the effect of the high tidal coherence along the second eigenvector direction shifts from the obstruction to the facilitation of the satellite infalls, depending on which eigenvector direction between the first and third the tides are simultaneously coherent. If the tides are highly coherent along none of the first and third eigenvector direction, then the high tidal coherence along the second eigenvector direction does not have a strong effect on the satellite infalls.

It is interesting to see that the tides highly coherent along all of the three eigenvector directions (red bar) are less effective in obstructing the satellite infalls than the tides highly coherent along the first and second eigenvector directions but not highly coherent along the third eigenvector direction (scarlet bar). It is even not so effective in obstructing the satellite infalls as the tides highly coherent only along the third eigenvector direction but not along the first and second eigenvector direction (thick violet bar). Note also that the second highest value of  $\langle \xi_m \rangle$  is found from the subsample with  $q_1 < 0.9, q_2 < 0.9, q_3 \geq 0.9$  (violet bar). Given that the mean ellipticity from this subsample is relatively low compared with the other seven cases (see Figure 10), this result implies that the net obstructing effect of the tides highly coherent only along the third but not along the first and second eigenvector directions may be stronger than that of the tides highly coherent only along the first and second eigenvector directions but not along the third eigenvector direction (scarlet bar).

As done in Subsections 2.2 and 2.3, we also investigate how the degree of the tidal *incoherence* measured along all of three eigenvector directions is linked with the subhalo mass-loss evolution, creating seven new subsamples by constraining simultaneously all of the three components,  $(q_1, q_2, q_3)$  with double thresholds of 0.9 and 0.2 (see Table 3): It turns out that no hosts satisfy the conditions of  $(q_1 \geq 0.9, q_2 < 0.2, q_3 < 0.2)$ ,  $(q_1 < 0.2, q_2 \geq 0.9, q_3 \geq 0.9)$  and  $(q_1 < 0.2, q_2 \geq 0.9, q_3 < 0.2)$ , leaving three subsamples empty. The values of  $(\langle \xi_m \rangle, \sigma_{\xi_m})$ ,  $(\langle \delta \rangle, \sigma_\delta)$  and  $(\langle e \rangle, \sigma_e)$  obtained from the rest four non-empty subsamples as well as from the subsample with  $(q_1 \geq 0.9, q_2 \geq 0.9, q_3 \geq 0.9)$  are shown in Figures 11-12.

The subsample with  $(q_1 \geq 0.9, q_2 < 0.2, q_3 < 0.2)$  yields the highest value of  $\langle \xi_m \rangle$  (olive green bar), while the lowest value (violet bar) is found from the subsample with  $(q_1 < 0.2, q_2 < 0.2, q_3 \geq 0.9)$ . Since the difference in  $\langle e \rangle$  between the two subsamples is not so large enough to explain their difference in  $\langle \xi_m \rangle$  (see Figure 12), the different mean ellipticities

between the two subsamples should not be the main cause of the significant difference in the mean virial-to-accretion mass ratios between them. The tides highly coherent along the first eigenvector direction but highly incoherent along the second and third eigenvector directions are much more effective in obstructing the satellite infalls than the tides highly coherent along the third eigenvector direction but highly incoherent along the first and second eigenvector directions.

The comparison of the result shown in Figures 9 and 11 reveals that the subsample with  $(q_1 < 0.9, q_2 \geq 0.9, q_3 \geq 0.9)$  yield a lower value of  $\langle \xi_m \rangle$  than the subsample with  $(q_1 < 0.2, q_2 < 0.2, q_3 \geq 0.9)$ . The tides highly coherent along the third eigenvector direction but highly *incoherent* along the first and second eigenvector direction are less effective in facilitating the satellite infalls than the tides highly coherent along the second and third eigenvector direction but not so highly coherent along the first eigenvector direction.

Another interesting fact revealed by the comparison between the two Figures is that the value  $\langle \xi_m \rangle$  from the subsample with  $(q_1 < 0.2, q_2 \geq 0.9, q_3 < 0.2)$  is as high as that from the subsample with  $(q_1 \geq 0.9, q_2 \geq 0.9, q_3 \geq 0.9)$ . This result indicates that the tides highly coherent only along the second eigenvector direction but highly *incoherent* along the first and third eigenvector directions are as effective in obstructing the satellite infalls as the tides highly *coherent* along all of the three eigenvector directions. It is a rather surprising unexpected result since we have already found in Subsection 2.2 that the tides highly coherent along the first eigenvector direction have an obstructing effect on the satellite infalls and that the tides highly *incoherent* along the same direction have the opposite effect, i.e., facilitating the satellite infalls. The slightly larger value of  $\langle e \rangle$  from the subsample with  $(q_1 < 0.2, q_2 \geq 0.9, q_3 < 0.2)$  than that from the subsample with  $(q_1 \geq 0.9, q_2 \geq 0.9, q_3 \geq 0.9)$  should be related to this puzzling phenomenon (see Figures 10-12). The tidal *incoherence* along the third eigenvector direction tends to increase the tidal anisotropy (i.e., mean ellipticity) which plays a role in increasing the value of  $\langle \xi_m \rangle$ , as shown in Subsection 2.2. The obstructing effect of the high tidal anisotropy caused by the tidal *incoherence* along the third eigenvector direction compensates the facilitating effect of the high *incoherence* of the tides along the first eigenvector direction.

### 3. Summary and Discussion

We have systematically studied the dependence of the subhalo mass-loss evolution on the multi-dimensional aspect of the tidal coherence by using the numerical datasets retrieved from the SMPDL (Klypin et al. 2016). For this study, we have quantified the subhalo mass-loss evolution in terms of the mean virial-to-accretion mass ratios averaged over the subhalos,

and expressed the tidal coherence as an array of three numbers,  $\{q_i\}_{i=1}^3$ , where  $q_i$  represents the alignments between the  $i$ th eigenvectors of the tidal fields smoothed on two widely separated scales of  $2 h^{-1}\text{Mpc}$  and  $30 h^{-1}\text{Mpc}$ . To eliminate the well known strong dependence of the subhalo mass-loss evolution on the masses of their hosts (van den Bosch et al. 2005), we select only those subhalos belonging to the hosts whose masses lie in the narrow range of  $1 \leq M_h/(10^{14} h^{-1} M_\odot) \leq 3$ .

It has been found that the subhalos surrounded by the tides highly coherent along a eigenvector direction ( $q_i \geq 0.9$ ,  $\forall i \in \{1, 2, 3\}$ ) tend to have higher mean values of the virial-to-accretion mass ratios than their counterparts ( $q_i < 0.9$ ), no matter what eigenvector direction is chosen. Our interpretation of this result is that the tides highly coherent along any eigenvector direction has an effect of obstructing the satellite infalls onto the hosts, which leads the satellites to experience the least severe mass-loss evolution in their post-infall stages. It has also been shown that the high tidal coherence along the third (second) eigenvector direction has the strongest (weakest) obstructing effect on the satellite infalls.

The tides highly *incoherent* along a different eigenvector direction, however, has turned out to have a different effect. The tides highly *incoherent* along the first eigenvector direction ( $q_1 < 0.2$ ) have an effect opposite to the tides coherent along the same direction ( $q_1 \geq 0.9$ ) on the subhalo mass-loss evolution: the former facilitates the satellite infalls while the latter obstructs them, leading the subhalos surrounded by the former to lose much larger amount of masses after the infalls than those surrounded by the latter. In fact, the subhalos surrounded by the tides highly *incoherent* along the first eigenvector direction have been found to yield the lowest mean virial-to-accretion mass ratios. Whereas, the tides highly *incoherent* along the third eigenvector direction ( $q_3 < 0.2$ ) have an effect of obstructing rather than facilitating the satellite infalls, similar to the tides highly coherent along the same direction ( $q_3 \geq 0.9$ ).

It is shown that the simultaneous coherence or *incoherence* of the tides along two or three eigenvector directions have more complex effects on the subhalo mass-loss evolution. The high tidal coherence along the first eigenvector direction has been found to be synergic with the high tidal *incoherence* along the minor eigenvector direction ( $q_1 \geq 0.9$  and  $q_3 < 0.2$ ) in obstructing the satellite-infalls, yielding the highest mean virial-to-accretion mass ratios of the subhalos. Whereas, the high tidal *incoherence* along the first eigenvector direction has turned out to be discordant with both of the high tidal coherence and *incoherence* along the third eigenvector direction in facilitating the satellite infalls. The high tidal coherence along the second eigenvector direction have turned out to be synergic with the high tidal coherence along the first eigenvector direction in obstructing the satellite infalls, provided that the tides are not so coherent along the third eigenvector direction. Meanwhile, provided that the tides are not so coherent along the first eigenvector direction, the high tidal coherence along the

second eigenvector direction has been found synergic with the high tidal coherence along the third eigenvector direction in facilitating the satellite infalls.

Although the tides highly coherent along one of the three eigenvector direction have an obstructing effect on the satellite infalls, the simultaneous coherence of the tides along all of the three eigenvector directions have been found not to reinforce the obstructing effect. The tides highly coherent along the first eigenvector direction and *incoherent* along the second and third eigenvector directions have been found more effective in obstructing the satellite infalls than the tides simultaneously coherent along all of the three eigenvector directions. The same is true for the simultaneous *incoherence* of the tides along all of the three eigenvector directions, which have been found not to reinforce the effect of facilitating the satellite infalls. The tides highly coherent along the third eigenvector direction and simultaneously *incoherent* along the first and second eigenvector direction have been found more effective in facilitating the satellite infalls than the tides simultaneously *incoherent* along all of the three eigenvector directions.

Determining the mean values of the local density contrasts,  $\langle\delta\rangle$ , and tidal anisotropies,  $\langle e\rangle$ , averaged over the regions with different tidal coherences, we have found negligible differences in  $\langle\delta\rangle$  and substantial differences in  $\langle e\rangle$  among the regions. Noting that the simultaneous coherence along all of the three eigenvector directions plays a significant role of reducing the tidal anisotropy, and recalling that the high tidal anisotropy has been known to obstruct the satellite infalls (e.g., Borzyszkowski et al. 2017), we have explained that the higher tidal anisotropy should be contributed to the stronger obstructing effect of the tides highly coherent along the first eigenvector direction but highly *incoherent* along the second and third eigenvector directions than the tides highly coherent along all of the three eigenvector directions. Yet, we have also shown that the multi-dimensional tidal coherence have an independent net effect on the subhalo-mass loss evolution, which cannot be ascribed simply to the differences in the tidal anisotropy.

Given that the mean virial-to-accretion mass ratios of the subhalos reflect not only their mass-loss evolutions but also how fast their host clusters have grown as well as in what dynamical states they are (van den Bosch et al. 2005), the bottom line of our work is as follows: The formation and evolution of the cluster halos at fixed mass scales located in the environments with similar densities and tidal anisotropies still show variations with the multi-dimensional effects of the tidal coherence. We suspect that this result may be responsible for the large scatters around the spherical critical density contrast of  $\delta_c \equiv 1.68$  required for the formation of a cluster halo, which could not be entirely explained by the scale-dependence of the non-spherical counter-part,  $\delta_{ec}$  (e.g., Maggiore, & Riotto 2010; Corasaniti, & Achitouv 2011). Our result may be also closely related to the elusive nature of the large-scale as-

sembly bias, whose existence have so far gained no observational confirmations (e.g., see Sunayama, & More 2019). It is not only the density and tidal strengths but also the multi-dimensional tidal coherence that we must take into account to detect the large-scale assembly bias. We plan to work on finding a direct link between the tidal coherence and the large-scale assembly bias as well as on extending the excursion set model by incorporating the tidal coherence, hoping to report the results elsewhere in the near future.

I acknowledge the support of the Basic Science Research Program through the National Research Foundation (NRF) of Korea funded by the Ministry of Education (NO. 2016R1D1A1A09918491). I was also partially supported by a research grant from the NRF of Korea to the Center for Galaxy Evolution Research (No.2017R1A5A1070354).

## REFERENCES

- Bardeen, J. M., Bond, J. R., Kaiser, N., et al. 1986, *ApJ*, 304, 15
- Behroozi, P. S., Wechsler, R. H., & Wu, H.-Y. 2013, *ApJ*, 762, 109
- Bond, J. R., Cole, S., Efstathiou, G., et al. 1991, *ApJ*, 379, 440
- Bond, J. R., & Myers, S. T. 1996, *ApJS*, 103, 1
- Bond, J. R., Kofman, L., & Pogosyan, D. 1996, *Nature*, 380, 603
- Borzyszkowski, M., Porciani, C., Romano-Díaz, E., & Garaldi, E. 2017, *MNRAS*, 469, 594
- Corasaniti, P. S., & Achitouv, I. 2011, *Phys. Rev. D*, 84, 023009
- Desjacques, V. 2008, *MNRAS*, 388, 638
- Ganeshaiiah Veena, P., Cautun, M., Tempel, E., et al. 2019, *MNRAS*, 487, 1607
- Gao, L., & White, S. D. M. 2007, *MNRAS*, 377, L5
- Garaldi, E., Romano-Díaz, E., Borzyszkowski, M., & Porciani, C. 2017, arXiv:1707.01108
- González, R. E., & Padilla, N. D. 2016, *ApJ*, 829, 58
- Hahn, O., Porciani, C., Carollo, C. M., & Dekel, A. 2007, *MNRAS*, 375, 489
- Hahn, O., Porciani, C., Dekel, A., et al. 2009, *MNRAS*, 398, 1742
- Klypin, A., Yepes, G., Gottlöber, S., Prada, F., & Heß, S. 2016, *MNRAS*, 457, 4340
- Lazeyras, T., Musso, M., & Schmidt, F. 2017, *JCAP*, 2017, 059
- Lee, J. 2019, *ApJ*, 872, L6
- Maggiore, M., & Riotto, A. 2010, *ApJ*, 717, 515
- Mansfield, P., & Kravtsov, A. V. 2019, arXiv e-prints, arXiv:1902.00030
- Musso, M., Cadiou, C., Pichon, C., et al. 2018, *MNRAS*, 476, 4877
- Obuljen, A., Dalal, N., & Percival, W. J. 2019, arXiv e-prints, arXiv:1906.11823
- Planck Collaboration, Ade, P. A. R., Aghanim, N., et al. 2014, *A&A*, 571, A16
- Plionis, M., & Basilakos, S. 2002, *MNRAS*, 329, L47

- Press, W. H., & Schechter, P. 1974, *ApJ*, 187, 425
- Ramakrishnan, S., Paranjape, A., Hahn, O., et al. 2019, arXiv e-prints, arXiv:1903.02007
- Sandvik, H. B., Möller, O., Lee, J., et al. 2007, *MNRAS*, 377, 234
- Sheth, R. K., Mo, H. J., & Tormen, G. 2001, *MNRAS*, 323, 1
- Sunayama, T., & More, S. 2019, arXiv e-prints, arXiv:1905.07557
- Tojeiro, R., Eardley, E., Peacock, J. A., et al. 2017, *MNRAS*, 470, 3720
- Wang, H., Mo, H. J., Jing, Y. P., et al. 2011, *MNRAS*, 413, 1973
- West, M. J., Jones, C., & Forman, W. 1995, *ApJ*, 451, L5
- van den Bosch, F. C., Tormen, G., & Giocoli, C. 2005, *MNRAS*, 359, 1029
- Vera-Ciro, C. A., Sales, L. V., Helmi, A., et al. 2011, *MNRAS*, 416, 1377
- Yang, X., Zhang, Y., Lu, T., et al. 2017, *ApJ*, 848, 60



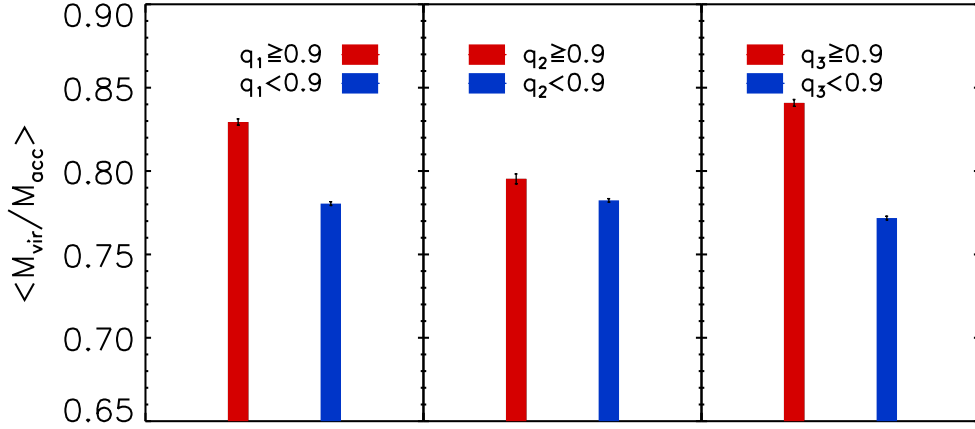


Fig. 1.— Mean virial-to-accretion mass ratios of the subhalos belonging to the hosts surrounded by the tides highly coherent along one of three eigenvector directions as red bar (major, intermediate and third eigenvector directions in the left, middle and right panels, respectively.) In each panel, the complement case of the tides not so highly coherent along the same direction is plotted as blue bar.

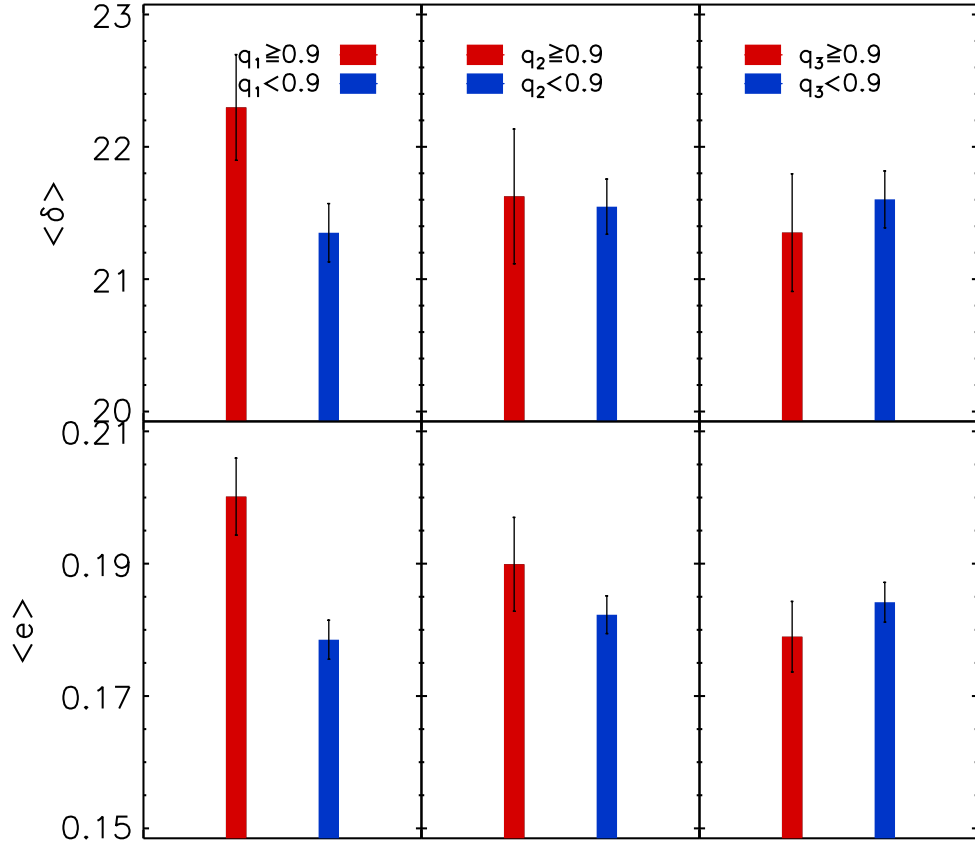


Fig. 2.— Mean values of the density contrast and ellipticity averaged over the regions surrounded by the tides highly coherent along one of three eigenvector directions as red bar in the top and bottom panels, respectively. In each panel, the blue bar correspond to the complement case.

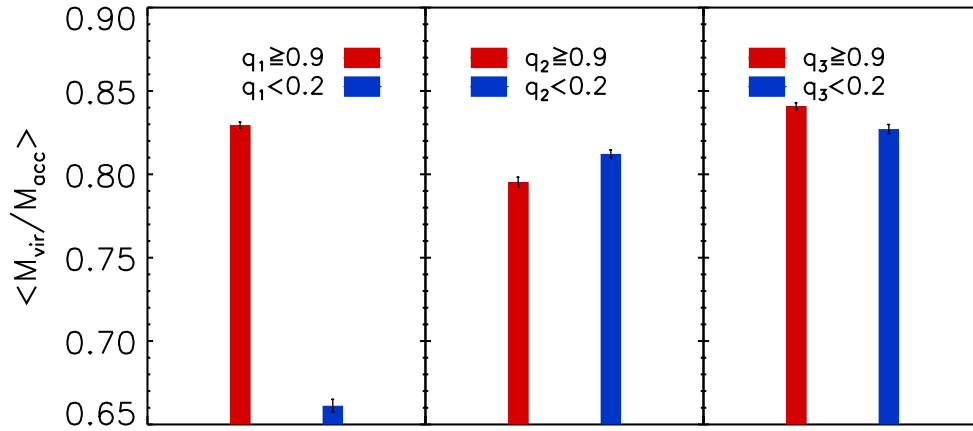


Fig. 3.— Mean virial-to-accretion mass ratios of the subhalos belonging to the hosts surrounded by the tides highly coherent (*incoherent*) along one of three eigenvector directions as red (blue) bar.

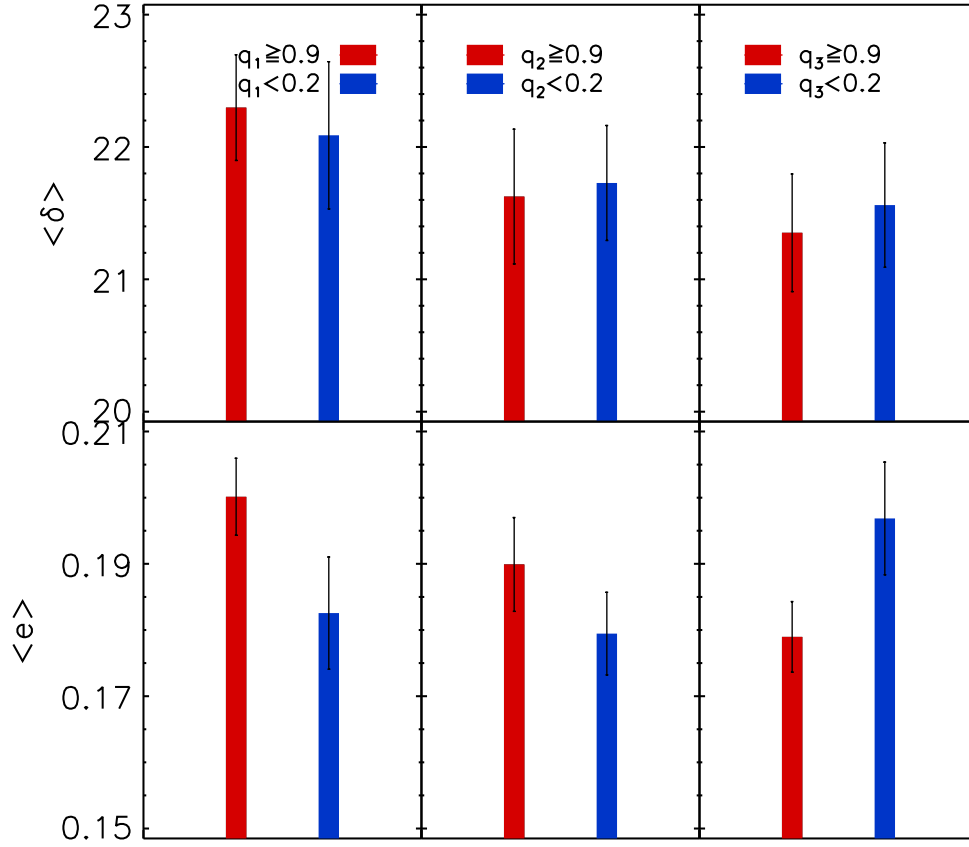


Fig. 4.— Mean values of the density contrast and ellipticity averaged over the regions surrounded by the tides highly coherent (*incoherent*) along one of three eigenvector directions as red (blue) bar in the top and left panels, respectively.

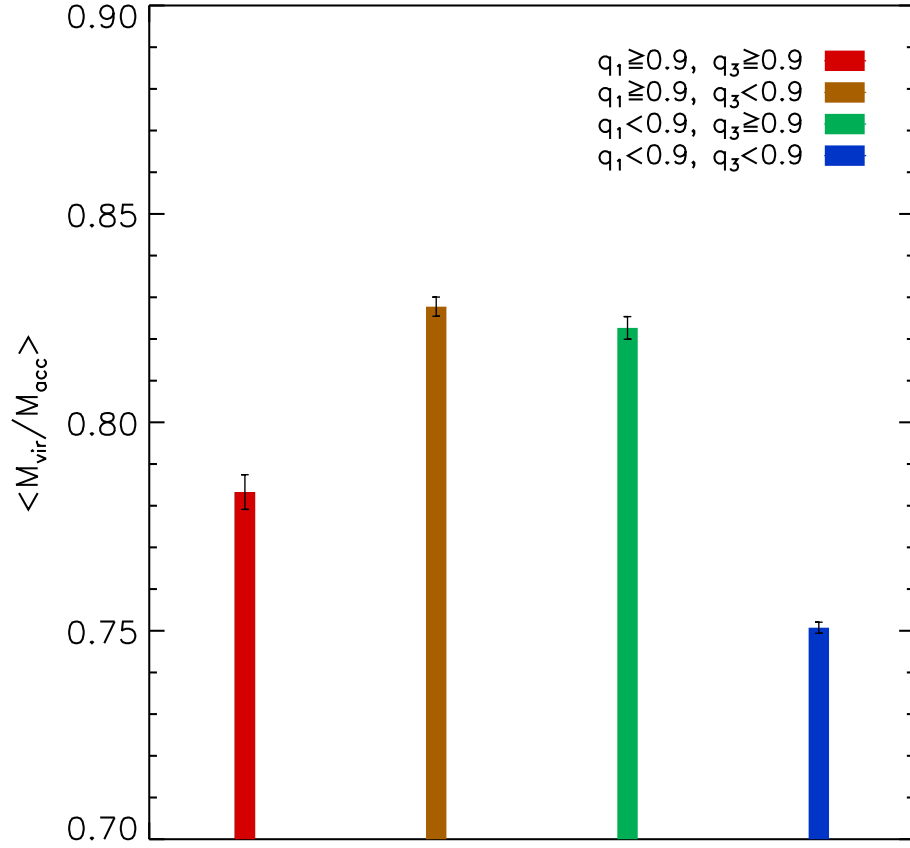


Fig. 5.— Mean virial-to-accretion mass ratios of the subhalos belonging to the hosts surrounded by the tides highly coherent along both of the first and third (thick red bar), along the first but not along the third (thick ocher bar), highly coherent along the third but not along the first (thick green bar), and highly coherent along none of the first and third eigenvector directions (thick blue bar).

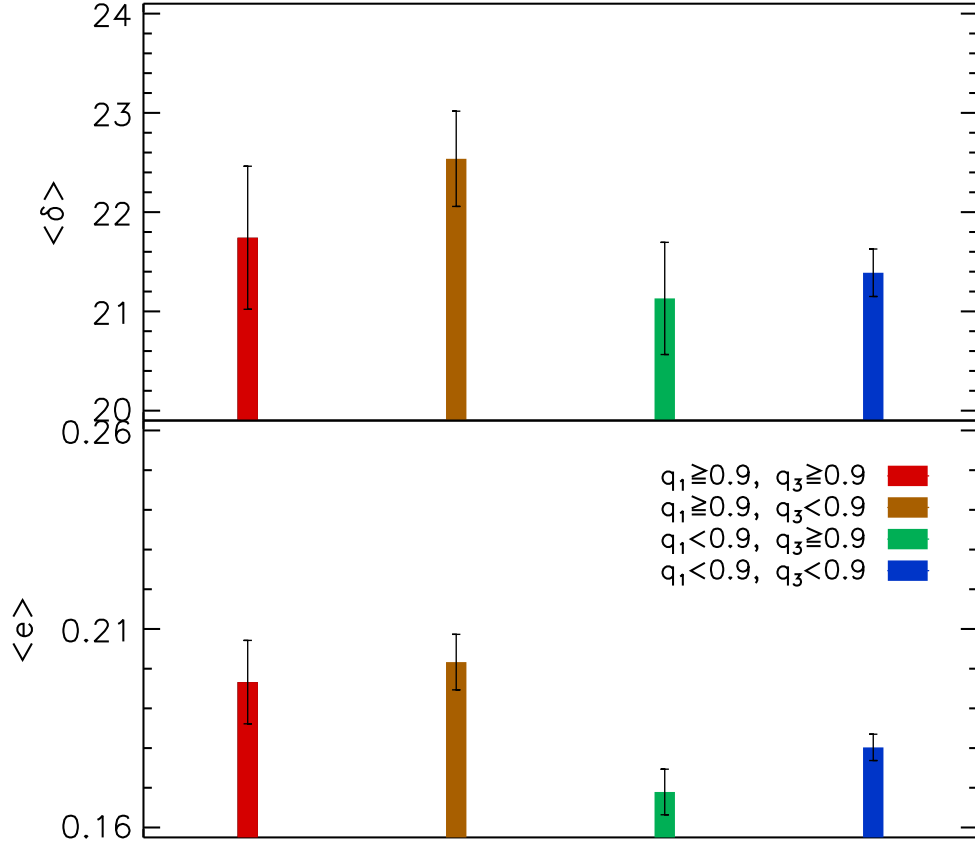


Fig. 6.— Mean values of the density contrast and ellipticity averaged over the regions surrounded by the tides for the four different cases described in the caption of Figure 5 in the top and bottom panels, respectively.

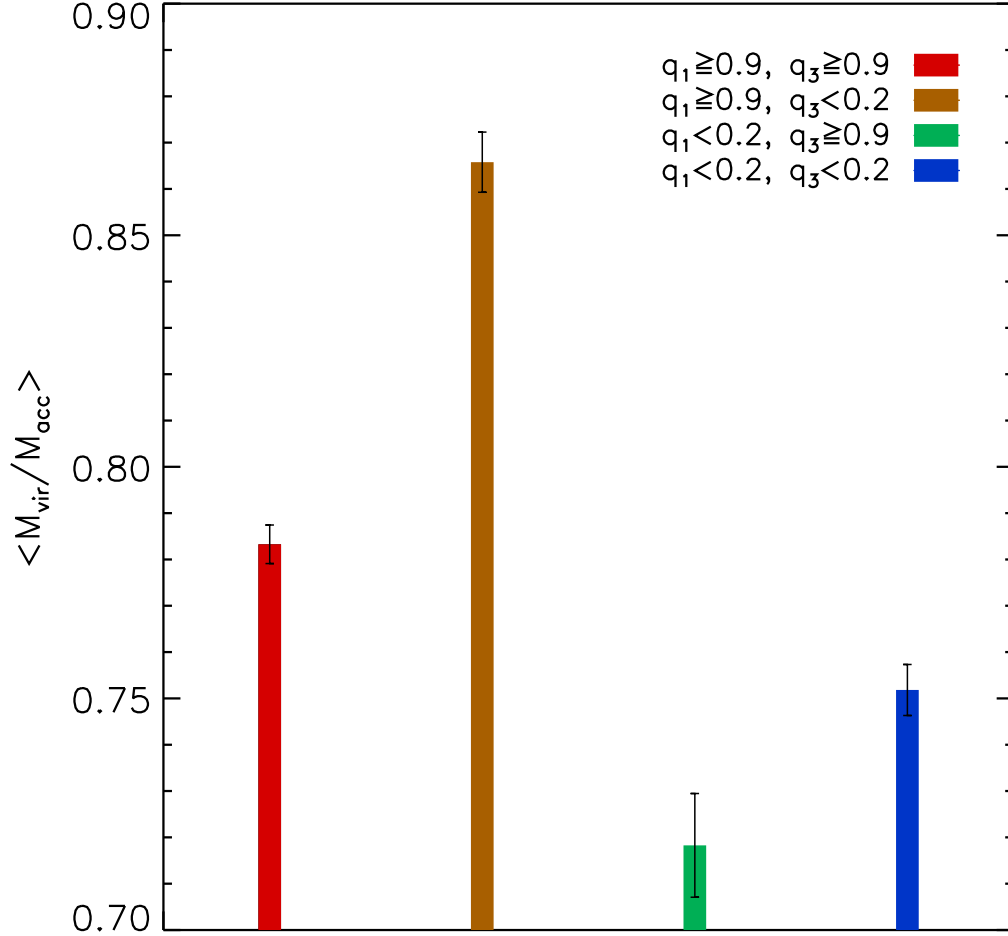


Fig. 7.— Mean virial-to-accretion mass ratios of the subhalos belonging to the hosts surrounded by the tides highly coherent along both of the first and third (red bar), highly coherent along the first but highly *incoherent* along the third (ocher bar), highly coherent along the third but highly *incoherent* along the first (green bar), and highly *incoherent* along the first and third eigenvector directions (blue bar).

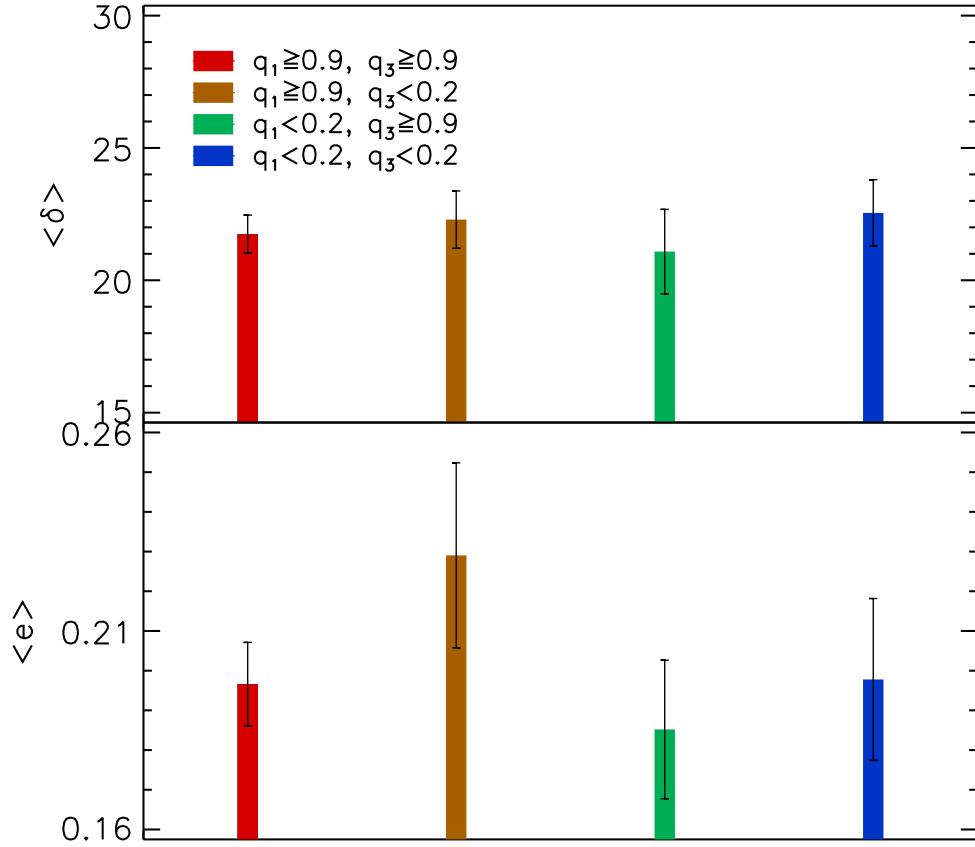


Fig. 8.— Mean values of the density contrast and ellipticity averaged over the regions surrounded by the tides for the four different cases described in the caption of Figure 7 in the top and bottom panels, respectively.



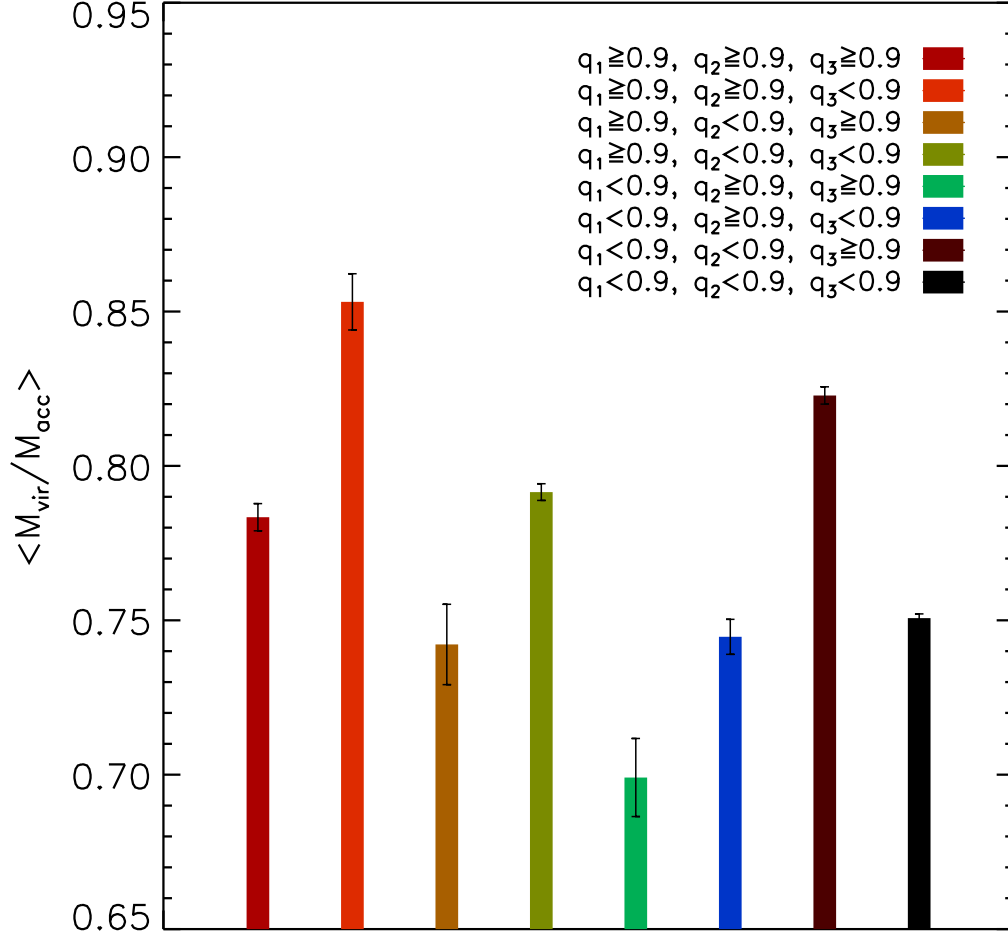


Fig. 9.— Mean virial-to-accretion mass ratios of the subhalos belonging to the hosts surrounded by the tides highly coherent along all of the three eigenvector directions are plotted as carmine bar. The seven complement cases corresponding to the tides coherent along not all of the three eigenvector directions are plotted as different color bars.

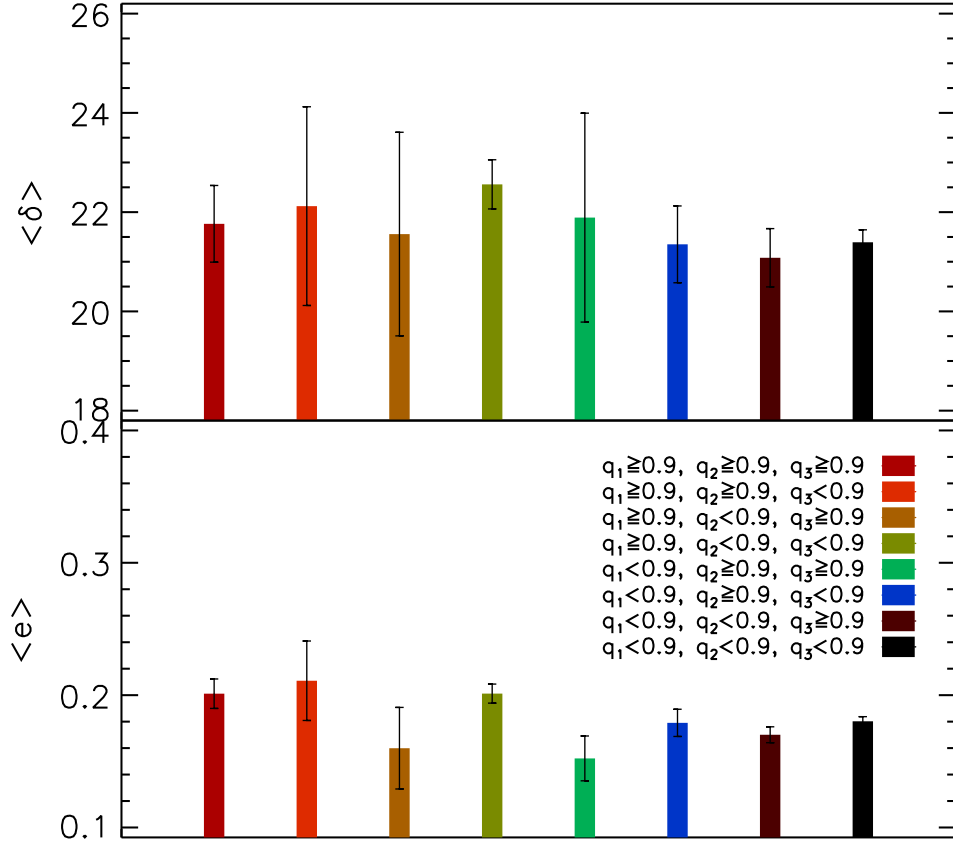


Fig. 10.— Mean values of the density contrast and ellipticity averaged over the regions surrounded by the tides for the eight different cases described in the caption of Figure 9 in the top and bottom panels, respectively.

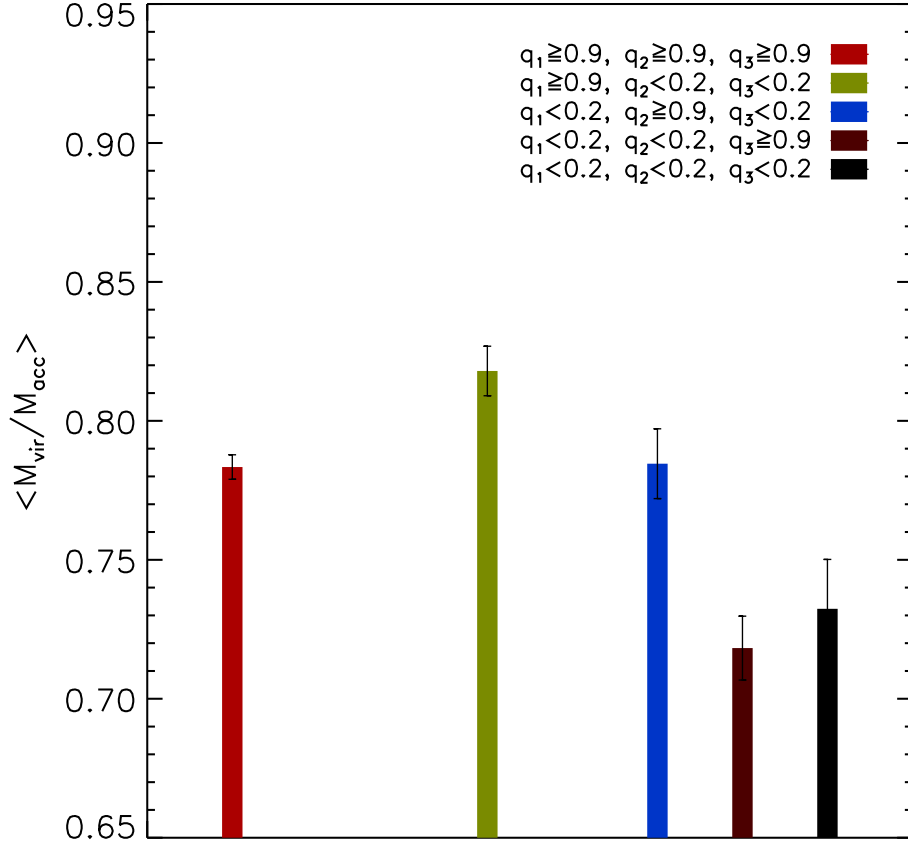


Fig. 11.— Mean virial-to-accretion mass ratios of the subhalos belonging to the hosts surrounded by the tides highly *incoherent* along all of the three eigenvector directions are plotted as black bar. For comparison, the case of the tides coherent along all of the three directions are also plotted as carmine bar. The results from the three cases of the tides highly *incoherent* along two of the three eigenvector directions but highly coherent along the other directions are plotted as different color bars.

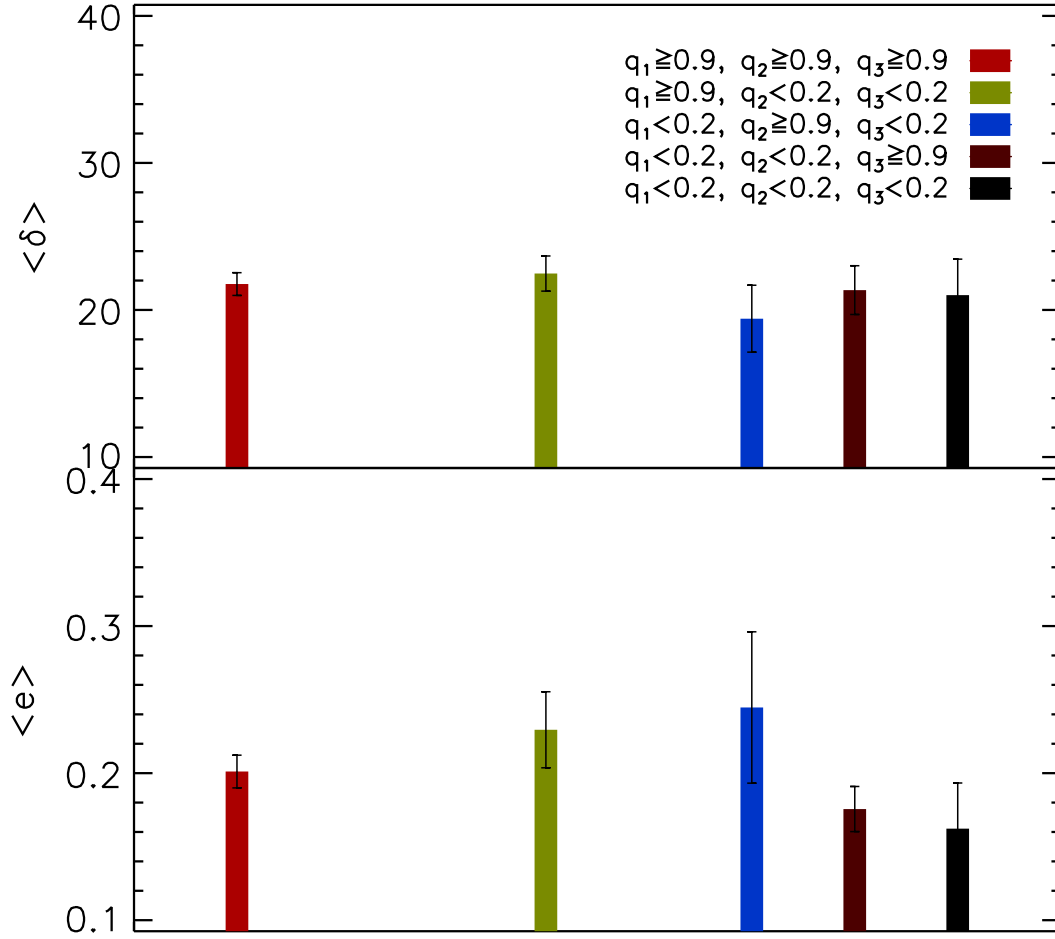


Fig. 12.— Mean values of the density contrast and ellipticity averaged over the regions surrounded by the tides for the five different cases described in the caption of Figure 11 in the top and bottom panels, respectively.

Table 1. 1D Tidal Coherence, Mean Mass and Number of the Hosts.

| condition      | $\langle M_h \rangle$<br>( $10^{14} h^{-1} M_\odot$ ) | $N_h$ |
|----------------|---|-------|
| $q_1 \geq 0.9$ | $1.63 \pm 0.03$                                       | 306   |
| $q_1 < 0.9$    | $1.58 \pm 0.02$                                       | 1096  |
| $q_1 < 0.2$    | $1.78 \pm 0.01$                                       | 179   |
| $q_2 \geq 0.9$ | $1.60 \pm 0.04$                                       | 174   |
| $q_2 < 0.9$    | $1.59 \pm 0.01$                                       | 1228  |
| $q_2 < 0.2$    | $1.75 \pm 0.01$                                       | 275   |
| $q_3 \geq 0.9$ | $1.60 \pm 0.03$                                       | 254   |
| $q_3 < 0.9$    | $1.59 \pm 0.02$                                       | 1148  |
| $q_3 < 0.2$    | $1.70 \pm 0.01$                                       | 203   |

Table 2. 2D Tidal Coherence, Mean Mass and Number of the Hosts.

| condition                    | $\langle M_h \rangle$<br>( $10^{14} h^{-1} M_\odot$ ) | $N_h$ |
|------------------------------|---|-------|
| $q_1 \geq 0.9, q_2 \geq 0.9$ | $1.62 \pm 0.06$                                       | 92    |
| $q_1 \geq 0.9, q_2 < 0.9$    | $1.63 \pm 0.04$                                       | 214   |
| $q_1 < 0.9, q_2 \geq 0.9$    | $1.59 \pm 0.04$                                       | 162   |
| $q_1 < 0.9, q_2 < 0.9$       | $1.58 \pm 0.02$                                       | 934   |
| $q_1 \geq 0.9, q_2 < 0.2$    | $1.58 \pm 0.08$                                       | 26    |
| $q_1 < 0.2, q_2 \geq 0.9$    | $1.42 \pm 0.19$                                       | 9     |
| $q_1 < 0.2, q_2 < 0.2$       | $1.63 \pm 0.06$                                       | 78    |

Table 3. 3D Tidal Coherence, Mean Mass and Number of the Hosts.

| condition                                  | $\langle M_h \rangle$<br>( $10^{14} h^{-1} M_\odot$ ) | $N_h$ |
|--|---|-------|
| $q_1 \geq 0.9, q_2 \geq 0.9, q_3 \geq 0.9$ | $1.61 \pm 0.06$                                       | 82    |
| $q_1 \geq 0.9, q_2 \geq 0.9, q_3 < 0.9$    | $1.65 \pm 0.17$                                       | 11    |
| $q_1 \geq 0.9, q_2 < 0.9, q_3 \geq 0.9$    | $1.73 \pm 0.19$                                       | 10    |
| $q_1 \geq 0.9, q_2 < 0.9, q_3 < 0.9$       | $1.64 \pm 0.04$                                       | 203   |
| $q_1 < 0.9, q_2 \geq 0.9, q_3 \geq 0.9$    | $1.61 \pm 0.16$                                       | 10    |
| $q_1 < 0.9, q_2 \geq 0.9, q_3 < 0.9$       | $1.62 \pm 0.06$                                       | 71    |
| $q_1 < 0.9, q_2 < 0.9, q_3 \geq 0.9$       | $1.59 \pm 0.04$                                       | 152   |
| $q_1 < 0.9, q_2 < 0.9, q_3 < 0.9$          | $1.57 \pm 0.02$                                       | 863   |
| $q_1 \geq 0.9, q_2 < 0.2, q_3 < 0.2$       | $1.54 \pm 0.09$                                       | 22    |
| $q_1 < 0.2, q_2 \geq 0.9, q_3 < 0.2$       | $1.42 \pm 0.19$                                       | 9     |
| $q_1 < 0.2, q_2 < 0.2, q_3 \geq 0.9$       | $1.58 \pm 0.12$                                       | 19    |
| $q_1 < 0.2, q_2 < 0.2, q_3 < 0.2$          | $1.61 \pm 0.17$                                       | 5     |